Model Predictive Control With Reduced Common-Mode Current for Transformerless Current-Source PMSM Drives

Cheng Xue, *Student Member, IEEE*, Li Ding, *Member, IEEE*, and Yunwei (Ryan) Li, *Fellow, IEEE*

***Abstract*—The integrated dc-link choke can replace the bulky transformer in current-source converter (CSC)-fed motor drive systems to bear the common-mode voltage (CMV). However, the common-mode (CM) resonance will be excited by the specific harmonics in the CMV, which causes excessive CM current in the loop. Moreover, due to the high-order filter, the LC/CL resonance is prone to be induced at the rectifier and inverter sides, respectively. In this article, the model predictive control (MPC) scheme is proposed to tackle the CM resonance and filter resonance simultaneously. In the low-speed region, besides restraining the peak-to-peak (PTP) magnitude of the CMV at the rectifier side, the third-order harmonic of the CMV generated by the inverter is extracted and then penalized in the cost function to further suppress the CM current. With the increase of the motor speed, the control objective of the inverter side controller switches to the PTP magnitude of CMV suppression because of the alleviation of the CM resonance. The capacitor voltage of both rectifier and inverter sides are regulated via the cost function as well, which can mitigate the current harmonic distortion and improve system stability. The simulation with 1MVA rated power and the scaled-down experiment shows that the proposed scheme can suppress both the CM resonance and the LC/CL resonance effectively with a low switching frequency.**

***Index Terms*—Common-mode (CM) current, CM resonance, capacitor voltage, common-mode voltage (CMV), cost function, current-source converter (CSC), LC/CL resonance, model predictive control (MPC), transformerless operation.**

I. Introduction

HIGH-power converters and medium-voltage (MV) variable-speed drive (VSD) systems have gained a widespread of applications such as large compressors, fans in the cement industry, and pumped hydro storage systems, etc. [1]. They still present an ever-growing trend because of the energy-saving advantage and the potential productivity in industrial automation. Multilevel voltage source converters (ML-VSC) are commonly adopted in the high-power motor drive system [2], [3]. However, with the increased number of switching devices, the control algorithm for ML-VSC becomes more complicated. Current-source converter (CSC) features simple converter configuration, low switching dv/dt, and reliable overcurrent protection, which could be a good alternative to ML-VSC in MV application [4].

Manuscript received May 28, 2020; revised November 5, 2020; accepted December 9, 2020. Date of publication December 17, 2020; date of current version March 5, 2021. This work was supported by the Natural Sciences and Engineering Research Council (NSERC) of Canada. Recommended for publication by Associate Editor R. Kennel. *(Corresponding author: Cheng Xue.)*

The authors are with the Department of Electrical and Computer Engineering, University of Alberta, Edmonton AB T6G 2V4, Canada (e-mail: cxue1@ualberta.ca; lding@ualberta.ca; yunwei.li@ualberta.ca).

Color versions of one or more figures in this article are available at https://doi.org/10.1109/TPEL.2020.3045652.

Digital Object Identifier 10.1109/TPEL.2020.3045652

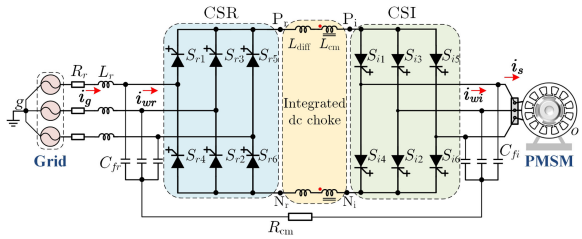

Fig. 1. Transformerless configuration of the CSC-fed PMSM drive system.

Fig. 1 shows the high-power transformerless configuration of the CSC-fed permanent-magnet synchronous motor (PMSM) drive system, where the converter utilizes the integrated gate-commutated thyristor (IGCT) as the switching device. The filter capacitor at both the current-source rectifier (CSR) and the current-source inverter (CSI) sides can refine the current waveforms while supporting the commutation of the switching devices. However, the inherent LC resonance is prone to be excited at the CSR side and the grid current oscillations will appear due to the low line impedance. Likewise, the CSI side output capacitor, together with the stator inductor of PMSM will cause the CL resonance in the motor current, which needs to be suppressed as well. The physical resistor can damp the LC/CL resonance but with the increased power loss and cost. Therefore, the virtual impedance (VR)-based active damping (AD) control scheme is increasingly being employed to improve the performance of LC/LCL filtered grid-connected VSC [5]–[7], CSC [8], [9], and CSC-fed PMSM drive system [10]. However, the VR-based AD scheme for CSC application needs the high-pass filter (HPF) to extract the harmonic component [11], which limits the bandwidth and increases the tuning complexity. Besides, the space vector modulation (SVM) for CSC with low switching frequency contains low-order harmonics in the modulated pulse, which usually leads to the 5th or 7th order harmonic [12].

Common-mode voltage (CMV) accompanied by the switching action is a major challenge for the motor drive system [2].

The CMV raises the voltage stress of the motor shaft with respect to the ground and induces the bearing current, which seriously threatens the lifetime of the motor [13]. The isolated transformer can shift the voltage stress but the system size is increased by 30–50% [2], [14]. Due to the superior harmonic profile, the selective harmonic elimination (SHE) scheme is usually employed in the CSC to eliminate the low-order harmonics [1]. However, the SHE scheme is difficult to be realized in real time. The existing design of SVM scheme design mainly focuses on the suppression of peak-to-peak (PTP) magnitude of CMV, such as the two-level VSC-fed induction motor (IM) [15], the neutral-point clamped (NPC) inverter-fed IM [16], the five-phase VSC-fed IM [17], and the CSC-fed IM [18]. All of these CMV reduction schemes select the switching state with low CMV to synthesize the reference vector. In [18], the SVM without using the zero-state vectors can reduce the PTP value of CMV in CSC-fed motor drive, but comes at the expense of deteriorating the power quality and increased switching frequency. Furthermore, an improved SVM was proposed with the mechanism that selects the zero-state vector with the minimum CMV at each sampling interval [19]. This way can achieve better system performance and reduced CMV. To realize the transformerless operation of the CSC-fed motor drive system, the total CMV can be approximately clamped to zero by directly connecting the neutral point of the input and the output capacitor [20], as shown in Fig. 1. To limit the CM current, the CM choke and the damped resistor are used to increase the impedance of the CM loop. Yet, the CM choke still represents a considerable size and weight of the system. Since the CM loop includes the inductive choke and two ac-side capacitors, the CM resonance will be excited by the CSI side CMV when the motor runs in the low-speed region [20]. As a result, a large CM current will be induced in the loop, which can cause the magnetic saturation of the CM choke. Therefore, it is still necessary to refine the waveform of the CMV although the transformerless operation is realized. Being different from previous work, the SVM scheme with the average value reduction (AVR) of the CSI side CMV was proposed in [21] to reduce the dominant third-order harmonic and thus to alleviate the CM resonance. This principle was subsequently extended to the parallel CSC system [22], [23]. However, the concept of AVR does not exist in some advanced control schemes, e.g., finite-control-set model predictive control (FCS-MPC) [24]. Recently, FCS-MPC has received great favor in power converter control, since the cost function provides great flexibility to handle system constraints and objectives with different physical dimensions [25]. Another benefit of FCS-MPC is the switching state can be directly manipulated without using an external modulator. In [26], the FCS-MPC for CSC-fed IM drive was investigated, where only the reduction of PTP magnitude of CMV is considered. Since no CM choke is used, the voltage stress on the motor is still very high. Besides, the LC/CL resonance problem is not addressed.

In this article, the FCS-MPC scheme is employed at both the CSR and the CSI sides to realize the multiobjective optimization. In the high-speed range, the PTP magnitude of the CMV from CSR and CSI sides are both suppressed through the cost function. While the control objective of the CSI side switches to suppress the third-order harmonic in the CMV when the motor runs in the low-speed range. The contribution of this article can be summarized as follows. First, compared to the CMV reduction results in [26], the transformerless operation is enabled in this article, which can significantly mitigate the voltage stress on the motor. The additional CM resonance problem is addressed and suppressed effectively by the proposed FCS-MPC scheme. Second, the size of the CM choke adopted can be reduced since the CM current is maintained at a low level in both the high-speed region and low-speed region. Third, the proposed method specifically controls the third-order harmonic of the CSI side CMV in the low-speed region, which has not been reported through the FCS-MPC strategy. Fourth, the proposed FCS-MPC solves the LC/CL resonance problem by directly regulating the capacitor voltage, which is not addressed in [26]. Compared to the multiloop feedback based AD schemes, the proposed method shows intuitive concept, easy realization, and improved bandwidth.

The rest of this article is organized as follows. The system setup and the control problems in transformerless CSC-fed PMSM drives are presented in Section II. Section III proposes the FCS-MPC framework for the CSC with LC/CL resonance suppression and the CM current reduction. Sections IV and V show the comparative simulated and experimental results, respectively, and these tests include operations in the low-speed region and the high-speed region, respectively. Finally, Section VI concludes this article.

II. System Setup and Control Problems

A. System Setup

In Fig. 1, the three-phase voltage and current of the grid are defined as $\boldsymbol{v_{gabc}} = [v_{ga}\ v_{gb}\ v_{gc}]^{\mathrm{T}}$ and $\boldsymbol{i_{gabc}} = [i_{ga}\ i_{gb}\ i_{gc}]^{\mathrm{T}}$, respectively. R_r is the line resistance and L_r, C_{fr} form the input filter at the CSR side. Likewise, the stator voltage and current of the PMSM are defined as $\boldsymbol{v_{sabc}} = [v_{sa}\ v_{sb}\ v_{sc}]^{\mathrm{T}}$ and $\boldsymbol{i_{sabc}} = [i_{sa}\ i_{sb}\ i_{sc}]^{\mathrm{T}}$, respectively. The capacitance C_{fi} and the stator inductance L_s form a second-order filter at the CSI side. The integrated dc-link choke, including the differential inductance L_{diff} and CM inductance L_{cm}, connects the CSR and CSI bridges. The neutral points of the capacitor at both sides are connected through the damped resistor R_{cm} to limit the CM current i_{cm}.

Both CSR and CSI share the same bridge configuration. Each converter contains six IGCT devices and can generate nine current vectors with six active-state vectors and three zero-state vectors [1]. The current vector of CSR and CSI are defined as $\boldsymbol{i_{wr}}$ and $\boldsymbol{i_{wi}}$ in stationary $\alpha\beta$ space with the switching state $[S_{r1}, S_{r3}, S_{r5}; S_{r4}, S_{r6}, S_{r2}]$ and $[S_{i1}, S_{i3}, S_{i5}; S_{i4}, S_{i6}, S_{i2}]$, respectively. Each switch has two states: "1" (ON) and "0" (OFF). The distribution of the current vectors in the $\alpha\beta$ frame is shown in Fig. 2 and the expression is

$$\begin{aligned}\boldsymbol{i_{wr(i)}} &= i_{wr(i)\alpha} + j i_{wr(i)\beta} \\ &= \frac{2}{3}(i_{wr(i)a} + \chi i_{wr(i)b} + \chi^2 i_{wr(i)c}) \end{aligned} \tag{1}$$

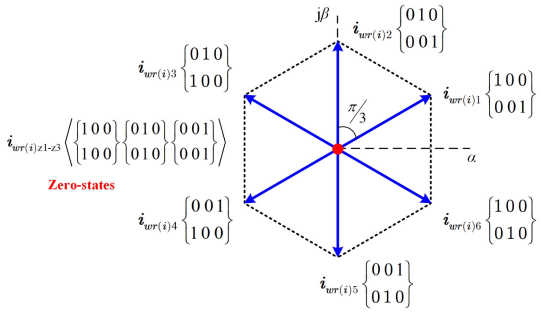

Fig. 2. Space vector diagram of CSC in the stationary $\alpha\beta$ frame.

where $\chi = \exp(j\frac{2\pi}{3})$. The three-phase converter current can be expressed as $i_{wr(i)a} = (S_{r(i)1} - S_{r(i)4})i_{dc}$, $i_{wr(i)b} = (S_{r(i)3} - S_{r(i)6})i_{dc}$ and $i_{wr(i)c} = (S_{r(i)5} - S_{r(i)2})i_{dc}$. The variable i_{dc} represents the dc-link current.

B. LC/CL Filter Resonance in CSC

Since the second-order filter is adopted for CSC, the dynamic between capacitor voltage and inductor current is a coupled process when the input variable is applied. Based on the filter model of CSR, the transfer function between grid current i_g and the input current i_{wr} in s-domain is derived as

$$\frac{\boldsymbol{i_g}(s)}{\boldsymbol{i_{wr}}(s)} = \frac{1}{s^2 L_r C_{fr} + sR_r C_{fr} + 1}. \tag{2}$$

A similar transfer function can be derived between the stator current $\boldsymbol{i_s}$ of PMSM and converter current $\boldsymbol{i_{wi}}$ of CSI. The transfer function (2) reveals that the resonance current peak mainly emerges at the frequency

$$f_{\text{LC\_res}} = \frac{1}{2\pi\sqrt{L_r C_{fr}}}\text{Hz}. \tag{3}$$

The harmonic distortion will appear in the grid current and the motor current. Because of the constant grid frequency, the LC filter of CSR will cause prominent 5th and 7th harmonic distortion in the grid current. While the harmonic order of stator current caused by the CL filter resonance will change with the motor speed. Therefore, to reduce the harmonic distortions in the grid current and the stator current, the control scheme for CSC-fed motor drive should be able to suppress the LC/CL filter resonance.

C. Expression and Properties of CMV Generated by CSC

The CMV generated by CSR and CSI sides are defined, respectively, as [21]

$$V_{\text{cmr}} = \frac{V_{\text{P}_r-g} + V_{\text{N}_r-g}}{2} \tag{4}$$

$$V_{\text{cmi}} = \frac{V_{\text{P}_i-o} + V_{\text{N}_i-o}}{2} \tag{5}$$

where V_{cmr} and V_{cmi} represent the CMV at CSR and CSI sides, respectively. V_{P_r-g} and V_{N_r-g} represent the voltage of two dc terminal P_r and N_r respectively, with respect to the ground g, as seen in Fig. 1. V_{P_i-o} and V_{N_i-o} represent the voltage of two dc terminal P_i and N_i, respectively, with respect to the neutral point o. Also, V_{cmr} and V_{cmi} can be calculated as [26]

$$V_{\text{cmr}} = \frac{1}{2}\cdot[S_{r1}+S_{r4} \;\; S_{r3}+S_{r6} \;\; S_{r5}+S_{r2}]\begin{bmatrix} v_{ga} \\ v_{gb} \\ v_{gc}\end{bmatrix} \tag{6}$$

$$V_{\text{cmi}} = \frac{1}{2}\cdot[S_{i1}+S_{i4} \;\; S_{i3}+S_{i6} \;\; S_{i5}+S_{i2}]\begin{bmatrix} v_{sa} \\ v_{sb} \\ v_{sc}\end{bmatrix}. \tag{7}$$

In (6), the capacitor voltage at the CSR side can be substituted with the grid voltage. Based on (6) and (7), it can be found that the CMV generated by the zero-switching state will be equal to the phase voltage while the active switching state will generate CMV magnitude with half of the phase voltage. Therefore, the overall shape of CMV is determined by the amplitude envelope of the capacitor voltage and the applied switching state.

In general, for the FCS-MPC scheme for CSC application, the transition between the active switching states is restrained to the adjacent vectors to limit large di/dt. Besides, since three redundant zero vectors exist in Fig. 2, the selection of zero vectors should follow the principle that maintains the minimum number of transitions with the previous switching state. For example, if the switching vector in the last interval is $\boldsymbol{i_{wr(i)1}}$ and a zero vector will be chosen, then $\boldsymbol{i_{wr(i)z1}}$ and $\boldsymbol{i_{wr(i)z3}}$ can be alternatives. However, these two zero-states are still redundant since there is no further control freedom to determine which one should be selected. Therefore, to ensure that the switching device of each phase can act evenly, the assignment of zero vector in the general FCS-MPC scheme can use the rule from the SVM strategy of CSC, where the transition of switching vectors is concluded in Table I.

To clearly show the property of the CMV generated by the CSC, the simulated waveform of the CMV and three-phase capacitor voltage of the CSI side is presented in Fig. 3, where the switching state is switched according to Table I (with simulated parameters in Table II). It can be found that the CMV shape is the envelope of the capacitor voltage. Besides, the CMV waveform contains the zero-sequence components and the dominant harmonic order is the third [21]. In the VSC

TABLE I
TRANSITION OF THE SWITCHING VECTORS FOR THE GENERAL FCS–MPC SCHEME

The vector in last interval	The candidate vectors in the next interval
$\boldsymbol{i_{wr(i)1}}$	$\boldsymbol{i_{wr(i)6}}$ $\boldsymbol{i_{wr(i)1}}$ $\boldsymbol{i_{wr(i)2}}$ $\boldsymbol{i_{wr(i)z3}}$
$\boldsymbol{i_{wr(i)2}}$	$\boldsymbol{i_{wr(i)1}}$ $\boldsymbol{i_{wr(i)2}}$ $\boldsymbol{i_{wr(i)3}}$ $\boldsymbol{i_{wr(i)z2}}$
$\boldsymbol{i_{wr(i)3}}$	$\boldsymbol{i_{wr(i)2}}$ $\boldsymbol{i_{wr(i)3}}$ $\boldsymbol{i_{wr(i)4}}$ $\boldsymbol{i_{wr(i)z1}}$
$\boldsymbol{i_{wr(i)4}}$	$\boldsymbol{i_{wr(i)3}}$ $\boldsymbol{i_{wr(i)4}}$ $\boldsymbol{i_{wr(i)5}}$ $\boldsymbol{i_{wr(i)z3}}$
$\boldsymbol{i_{wr(i)5}}$	$\boldsymbol{i_{wr(i)4}}$ $\boldsymbol{i_{wr(i)5}}$ $\boldsymbol{i_{wr(i)6}}$ $\boldsymbol{i_{wr(i)z2}}$
$\boldsymbol{i_{wr(i)6}}$	$\boldsymbol{i_{wr(i)5}}$ $\boldsymbol{i_{wr(i)6}}$ $\boldsymbol{i_{wr(i)1}}$ $\boldsymbol{i_{wr(i)z1}}$
$\boldsymbol{i_{wr(i)z1}}$	$\boldsymbol{i_{wr(i)1}}$ $\boldsymbol{i_{wr(i)3}}$ $\boldsymbol{i_{wr(i)4}}$ $\boldsymbol{i_{wr(i)6}}$ $\boldsymbol{i_{wr(i)z1}}$
$\boldsymbol{i_{wr(i)z2}}$	$\boldsymbol{i_{wr(i)2}}$ $\boldsymbol{i_{wr(i)3}}$ $\boldsymbol{i_{wr(i)5}}$ $\boldsymbol{i_{wr(i)6}}$ $\boldsymbol{i_{wr(i)z2}}$
$\boldsymbol{i_{wr(i)z3}}$	$\boldsymbol{i_{wr(i)1}}$ $\boldsymbol{i_{wr(i)2}}$ $\boldsymbol{i_{wr(i)4}}$ $\boldsymbol{i_{wr(i)5}}$ $\boldsymbol{i_{wr(i)z3}}$

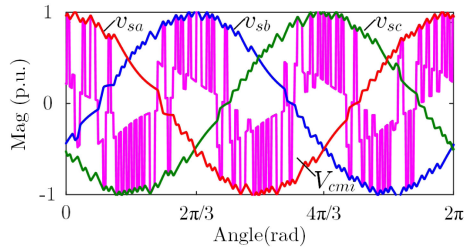

Fig. 3. Typical waveform of the CMV at the CSI side.

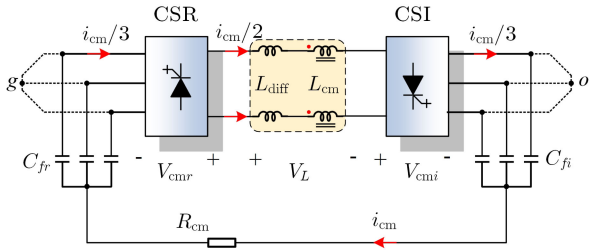

Fig. 4. CM loop in the transformerless CSC-fed PMSM drive.

TABLE II
SIMULATED PARAMETERS OF THE TRANSFORMERLESS DRIVE SYSTEM

	Parameters	Value
CSR	Grid voltage (line-to-line)	4160V
	Nominal power	1MVA
	Grid frequency	60Hz
	Line inductance L_r	4.58mH
	Input filter capacitance C_{fr}	76.64μF
DC link	Differential-mode inductance L_{diff}	31.5mH
	Common-mode inductance L_{cm}	400mH
	CM resistance R_{cm}	15Ω
	CM resonance frequency f_{cm_res}	30Hz
CSI-PMSM	Output capacitance C_{fi}	46μF
	Rated power of PMSM	1MVA
	Rated stator frequency	80Hz
	Rated torque of PMSM	8000N·m
	Stator inductance L_s	5.46mH
	Permanent fluxψ_f	8.45Wb
	Pole pairsψ_f	4
	Monent of inertia J	18kg·m^2

application, since the CMV is determined by the constant dc-link voltage and the applied switching state, the CMV spikes will be caused by the additional switching state due to the dead-time effect. On the contrary, the CMV waveform affected by the overlap time in CSC is not serious, since the CMV will be either smoothly maintained as the previous state or directly shifted to the upcoming state.

D. Transformerless Operation and CM Resonance

The CMV in the MV drive system can be blocked by the isolated transformer but with the expense of system cost and weight. The integrated dc-link choke, including differential inductance and CM inductance, has been proposed in [20] to replace the isolated transformer. The L_{diff} can reduce the dc-link current ripple while the L_{cm} is responsible for CMV suppression and the CM current limitation. According to Fig. 2, the CM loop is redrawn in Fig. 4, which essentially is an RLC circuit. As can be seen, V_{cmr} and V_{cmi} are the two voltage sources in the CM loop. Therefore, according to the Kirchhhoff voltage law, the whole CMV of the drive system V_{og}, namely the voltage between the neutral point o of the PMSM with respect to the ground g can be expressed as

$$V_{og} = V_{\text{cmr}} - V_{\text{cmi}} - V_L \tag{8}$$

where V_L represents the voltage drop on the integrated dc-link choke. The total CMV V_{og} can be significantly reduced since the dominant voltage component of V_{cmr}-V_{cmi} is canceled out by V_L. Moreover, the CM current i_{cm} can be calculated as

$$i_{\text{cm}} = \frac{V_{\text{cmr}} - V_{\text{cmi}}}{Z_{\text{cm}}} \tag{9}$$

where Z_{cm} is the total impedance of the CM loop. Therefore, the CM current i_{cm}will be entirely determined by V_{cmr}, V_{cmi}, and Z_{cm}. It should be pointed out that the positive/negative rail only contains half of the total CM current flowing in the same direction [20]. According to the properties of the CMV for the CSC, the third-order harmonic voltage is the dominant component in both V_{cmr} and V_{cmi}, i.e., $V_{\text{cmr\_3}}$ and $V_{\text{cmi\_3}}$. Thus, it can be deduced that i_{cm} will contain the dominant component with triple stator frequency of the motor and 180 Hz component (the grid frequency is 60 Hz).

The CM loop contains the inductive choke and two side capacitors of the CSC, which implies the CM series resonance will be easily excited by the CMV component with a specific frequency. The resonant frequency can be calculated as [20]

$$\begin{cases} f_{\text{cm\_}res} = \frac{1}{2\pi\sqrt{L_{\text{eq}}C_{\text{eq}}}}\text{Hz} \\ L_{\text{eq}} = L_{\text{cm}} + \frac{L_{\text{diff}}}{2} \\ C_{\text{eq}} = 3 \cdot \frac{C_{fr}\cdot C_{fi}}{C_{fr}+C_{fi}} \end{cases} \tag{10}$$

where L_{eq} and C_{eq} represent, respectively the equivalent inductance and capacitance of the CM loop. As shown in [20], the typical resonance frequency of the CM loop is designed in the range of 0.528–0.744 p.u., namely, $f_{\text{cm\_res}} = 31.5\sim44.7$ Hz.

The frequency of $V_{\text{cmr\_3}}$ is constant at 180 Hz, which is higher than the resonant frequency $f_{\text{cm\_res}}$. Therefore, the CM current induced by the CSR side is not very severe, since the CMV component with 180 Hz can be blocked by the CM choke. However, due to the speed of the motor changing, the frequency of $V_{\text{cmi\_3}}$ will change correspondingly. Assuming that the stator frequency of the motor is approximately kept at 10–15 Hz, the prominent third-order component with frequency 30–45 Hz will appear in V_{cmi}. As a result, the severe CM current will be induced in the CM loop, which may cause the magnetic saturation of the CM choke. Furthermore, the CMV stress on the motor will increase and the insulation challenge will be produced [21].

The core size of the CM choke is directly related to the PTP magnitude of $i_{\rm cm}$. As investigated in [27], if a toroid core is adopted and the PTP magnitude of $i_{\rm cm}$ is reduced by half, the core cross-sectional area, mean length per turn, and total copper loss of the choke can be reduced by 60%, 37%, and 22.25% respectively, which contributes to the reduction of the CM choke size.

III. Proposed FCS–MPC Scheme

The current reference tracking should be realized at both CSR and CSI sides, which ensures the power transmission and the normal operation of PMSM. Moreover, the CM resonance should be suppressed in the control scheme to minimize the CM current for the transformerless operation.

A. Predictive Model of Grid-Connected CSR

The control strategy for the CSR side can be executed under the $\alpha\beta$ frame without using the phase-locked loop block. The abc three-phase variable can be transformed into the $\alpha\beta$ reference frame by Clarke transformation. The grid current $\boldsymbol{i_g}=[i_{g\alpha}\, i_{g\beta}]^{\rm T}$ and capacitor voltage $\boldsymbol{v_{cr}}=[v_{cr\alpha}\, v_{cr\beta}]^{\rm T}$ are selected as the state variables. According to the Kirchhoff voltage and current laws, the state-space model of the LC filter can be described by the following continuous-time equation:

$$\frac{d\boldsymbol{x_r}}{dt}=\mathbf{A_r}\boldsymbol{x_r}+\mathbf{B_r}\boldsymbol{u_r} \tag{11}$$

where $\boldsymbol{x_r}=[i_{g\alpha}\ i_{g\beta}\ v_{cr\alpha}\ v_{cr\beta}]^{\rm T}$. The input vector aggregates CSR current $\boldsymbol{i_{wr}}$ and disturbance grid voltage $\boldsymbol{v_g}$, i.e., $\boldsymbol{u_r}=[i_{wr\alpha}\ i_{wr\beta}\ v_{g\alpha}\ v_{g\beta}]^{\rm T}$. The matrix $\mathbf{A_r}$ and $\mathbf{B_r}$ are given by

$$\mathbf{A_r}=\begin{bmatrix} -\frac{R_r}{L_r} & 0 & -\frac{1}{L_r} & 0 \\ 0 & -\frac{R_r}{L_r} & 0 & -\frac{1}{L_r} \\ \frac{1}{C_{fr}} & 0 & 0 & 0 \\ 0 & \frac{1}{C_{fr}} & 0 & 0 \end{bmatrix}$$

$$\mathbf{B_r}=\begin{bmatrix} 0 & 0 & \frac{1}{L_r} & 0 \\ 0 & 0 & 0 & \frac{1}{L_r} \\ -\frac{1}{C_{fr}} & 0 & 0 & 0 \\ 0 & -\frac{1}{C_{fr}} & 0 & 0 \end{bmatrix}.$$

According to the zero-order-hold principle, the continuous-time equation (11) can be discretized to obtain the predictive state equation as

$$\boldsymbol{x_r}(k+1)=\mathbf{G_r}\boldsymbol{x_r}(k)+\mathbf{H_r}\boldsymbol{u}_r(k) \tag{12}$$

where $\mathbf{G_r}=\exp(\mathbf{A_r}T_s)$, $\mathbf{H_r}=(\mathbf{G_r}-\mathbf{I_r})\mathbf{A_r}^{-1}\mathbf{B_r}$ and $\mathbf{I_r}$ is the identity matrix with the same dimension of $\mathbf{G_r}$. T_s denotes the duration of the sampling interval. Considering the one-step delay in the digital controller, the prediction of the state variable should move forward by one-step correspondingly [28], i.e., the predictive variable at k+2 instant will be evaluated in the cost function.

B. Cost Function Design for CSR Side

The objective of the CSR side is to ensure the grid power transmission and realize the sinusoidal grid current with low harmonic distortion. The reference of grid current can be generated according to the active power command P^* and reactive power command Q^* as

$$\begin{cases} i^*_{g\alpha}=\frac{2}{3}\frac{P^*v_{g\alpha}+Q^*v_{g\beta}}{v^2_{g\alpha}+v^2_{g\beta}} \\ i^*_{g\beta}=\frac{2}{3}\frac{P^*v_{g\alpha}-Q^*v_{g\beta}}{v^2_{g\alpha}+v^2_{g\beta}}. \end{cases} \tag{13}$$

Furthermore, the reference of capacitor voltage can be further derived as

$$\begin{cases} v^*_{cr\alpha}=v_{g\alpha}+\omega_g L_f i^*_{g\beta} \\ v^*_{cr\beta}=v_{g\beta}-\omega_g L_f i^*_{g\alpha} \end{cases} \tag{14}$$

where ω_g is the grid angular frequency. To suppress the LC filter resonance, both the grid current and capacitor voltage should be taken as the feedback simultaneously [8]. Therefore, the grid current and the capacitor voltage tracking at the CSR side are regulated simultaneously through [29]

$$\begin{aligned} g_{\rm CSR1}=&\left[i^*_{g\alpha}-i_{g\alpha}(k+2)\right]^2+\left[i^*_{g\beta}-i_{g\beta}(k+2)\right]^2 \\ &+\lambda_{V_{cr}}\left\{\left[v^*_{cr\alpha}-v_{cr\alpha}(k+2)\right]^2+\left[v^*_{cr\beta}-v_{cr\beta}(k+2)\right]^2\right\} \\ &+\lambda_{sfr}\left|i_{wr}(k+1)-i_{wr}(k)\right| \end{aligned} \tag{15}$$

where the positive weighting factor $\lambda_{V_{cr}}$ and λ_{sfr} are used to adjust the priority of capacitor voltage tracking and the penalization for switching frequency, respectively. Because the frequency of dominant component $V_{\rm cmr\_3}$ is constant at 180 Hz and the amplitude of grid voltage is constant as well, the component of $i_{\rm cm}$ induced by $V_{\rm cmr}$ will not change much. The peak of $i_{\rm cm}$ can be reduced if the PTP magnitude of $V_{\rm cmr}$ is suppressed well. In this case, the cost function is designed as the following to limit the PTP magnitude of $V_{\rm cmr}$:

$$g_{\rm CSR2}=\lambda_{V_{\rm cmr}}\left|V_{\rm cmr}(k+1)\right| \tag{16}$$

where $\lambda_{V_{\rm cmr}}$ is the positive weighting factor for the penalization of PTP magnitude of $V_{\rm cmr}$. The predictive $V_{\rm cmr}$ can be calculated according to the definition in (6). Based on (15) and (16), the unified cost function for the CSR side can be written as

$$g_{\rm CSR}=g_{\rm CSR1}+g_{\rm CSR2}. \tag{17}$$

The switching state is selected according to (17), which can track the current and capacitor voltage references and reduce the PTP magnitude of $V_{\rm cmr}$. As a result, the PTP value of $i_{\rm cm}$ can be reduced.

C. Predictive Model of CSI Fed-PMSM Drive

The $\alpha\beta$ stationary variable can be transformed into rotary dq reference frame with $\xi_{dq}=T_{\alpha\beta 2dq}\xi_{\alpha\beta}$, and the matrix $T_{\alpha\beta 2dq}$ is

$$T_{\alpha\beta 2dq}=\begin{bmatrix} \cos\theta_e & \sin\theta_e \\ -\sin\theta_e & \cos\theta_e \end{bmatrix} \tag{18}$$

where θ_e is the electrical angle. In dq frame, the three-phase quantities will be constant value under steady-state. For the

surface-mounted PMSMs, the dynamic model of stator current in dq reference frame is expressed as

$$\begin{cases} \frac{di_{sd}}{dt} = \frac{1}{L_s}(v_{sd} - R_s i_{sd} + \omega_e L_s i_{sq}) \\ \frac{di_{sq}}{dt} = \frac{1}{L_s}(v_{sq} - R_s i_{sq} - \omega_e L_s i_{sd} - \omega_e \psi_f) \end{cases} \tag{19}$$

where R_s is the stator resistor and ψ_f represents the magnitude of rotor flux ψ_r. ω_e is the electrical angular velocity and can be obtained through the encoder. For the CSI side, the dynamic model of the CL filter can be expressed as

$$\begin{cases} \frac{dv_{sd}}{dt} = \frac{1}{C_{fi}}\left(i_{wd} - i_{sd} + \omega_e C_{f_i} v_{sq}\right) \\ \frac{dv_{sq}}{dt} = \frac{1}{C_{fi}}\left(i_{wq} - i_{sq} - \omega_e C_{f_i} v_{sd}\right). \end{cases} \tag{20}$$

Based on (19) and (20), the state-space model of the CSI-fed PMSM in continuous-domain can be summarized as

$$\frac{d\boldsymbol{x_i}}{dt} = \mathbf{A_i}\boldsymbol{x_i} + \mathbf{B_i}\boldsymbol{u_i} \tag{21}$$

where the state vector $\boldsymbol{x_i} = [i_{sd}\ i_{sq}\ v_{sd}\ v_{sq}]^{\mathrm{T}}$. The input vector includes CSI current $\boldsymbol{i_{wi}}$ and ψ_f, namely $\boldsymbol{u_i} = [i_{wd}\ i_{wrq}\ \psi_f\ 0]^{\mathrm{T}}$. The current vector $\boldsymbol{i_{wi}}$ is determined by the dc-link current and the applied switching state. The time-varying matrix $\mathbf{A_i}$ and $\mathbf{B_i}$ are given by

$$\mathbf{A_i} = \begin{bmatrix} -\frac{R_s}{L_s} & \omega_e & \frac{1}{L_s} & 0 \\ -\omega_e & -\frac{R_s}{L_s} & 0 & \frac{1}{L_s} \\ -\frac{1}{C_f} & 0 & 0 & \omega_e \\ 0 & -\frac{1}{C_f} & -\omega_e & 0 \end{bmatrix}$$

$$\mathbf{B_i} = \begin{bmatrix} \frac{1}{C_f} & 0 & 0 & 0 \\ 0 & \frac{1}{C_f} & 0 & 0 \\ 0 & 0 & 0 & 0 \\ 0 & 0 & -\frac{\omega_e}{L_s} & 0 \end{bmatrix}.$$

Likewise, the continuous-time equation (21) can be discretized to obtain the predictive form (22) with the assumption that the input $\boldsymbol{u_i}$ is constant during each control interval

$$\boldsymbol{x_i}(k+1) = \mathbf{G_i}\boldsymbol{x_i}(k) + \mathbf{H_i}\boldsymbol{u_i}(k) \tag{22}$$

where $\mathbf{G_i} = \exp(\mathbf{A_i}T_s)$, $\mathbf{H_i} = (\mathbf{G_i} - \mathbf{I_i})\mathbf{A_i}^{-1}\mathbf{B_i}$ and $\mathbf{I_i}$ is the identity matrix with the same dimension of $\mathbf{G_i}$. Also, the predictive variable at k+1 instant will be compensated and then the cost function of the CSI side will evaluate the predictive information $\boldsymbol{x_i}(k+2)$.

D. Cost Function Design for CSI Fed-PMSM Drive

The electromagnetic torque T_e and stator flux ψ_s can be controlled implicitly by regulating the stator current of PMSM. However, because the CL resonance may occur and cause harmonic distortion, the feedback of stator voltage (capacitor voltage) should be introduced into the cost function as well. Therefore, the first component of the cost function for the CSI side is designed as

$$\begin{aligned} g_{\mathrm{CSI1}} = {} & [i_{sd}^* - i_{sd}(k+2)]^2 + \left[i_{sq}^* - i_{sq}(k+2)\right]^2 \\ & + \lambda_{V_s}\left\{[v_{sd}^* - v_{sd}(k+2)]^2 + \left[v_{sq}^* - v_{sq}(k+2)\right]^2\right\} \\ & + \lambda_{sfi}\left|i_{wi}(k+1) - i_{wi}(k)\right| \end{aligned} \tag{23}$$

where the third item penalizes the switching frequency with the weighting factor λ_{sfi}. The q-axis reference i_{sq}^* comes from the outer proportional–integral (PI) loop for motor speed regulation and the d-axis reference i_{sd}^* is set as 0 to achieve the operation with the maximum torque current ratio. The positive weighting factor $\lambda_{V_{ci}}$ is used to tune the priority of stator voltage tracking and thus the filter resonance can be controlled. The steady-state reference of stator voltage can be derived as

$$\begin{cases} v_{sd}^* = R_s i_{sd}^* - \omega_e L_s i_{sq}^* \\ v_{sq}^* = R_s i_{sq}^* + \omega_e L_s i_{sd}^* + \omega_e \psi_f. \end{cases} \tag{24}$$

Since the CM resonance will be excited by V_{cmi} when the motor runs in the low-speed region, the CMV control strategy is different from that of the CSR side, where only the PTP magnitude is suppressed in (17). The CM current will be mainly amplified by the third-order component $V_{\mathrm{cmi\_3}}$. Therefore, it is important to eliminate $V_{\mathrm{cmi\_3}}$ when the motor runs at the low-speed. To achieve this goal, the cost function is designed as follows to limit $V_{\mathrm{cmi\_3}}$ but not the PTP magnitude of V_{cmi} in the low-speed region

$$g_{\mathrm{CSI2\_LS}} = \lambda_{V_{\mathrm{cmi\_3}}}\left|V_{\mathrm{cmi\_3}}(k+1)\right| \tag{25}$$

where $\lambda_{V_{\mathrm{cmi\_3}}}$ is the positive weighting factor for the penalization of the magnitude of $V_{\mathrm{cmi\_3}}$. As can be seen in (25), to effectively suppress the magnitude of $V_{\mathrm{cmi\_3}}$, the extraction of harmonic information is needed. The sliding discrete Fourier transform (SDFT) strategy [30] can be employed to predict the harmonic information and be realized in real-time with a low computational cost. The principle of SDFT is to store the data of the signal into a buffer with a constant dimension. With the signal updated, the new predictive data of the signal is sent into the buffer while the first data in the buffer is discarded. Based on the recursive expression

$$\begin{aligned} |V_{\mathrm{cmi\_}h}(k+1)| = {} & |V_{\mathrm{cmi\_}h}(k)|\, \mathrm{e}^{j\frac{2\pi h}{N}} \\ & - V_{\mathrm{cmi}}(k+1-N) + V_{\mathrm{cmi}}(k+1) \end{aligned} \tag{26}$$

the predictive harmonic component can be calculated, where the positive integer h refers to the extracted harmonic order of V_{cmi}, i.e., $h = 3$.

As the motor speed increases, the CM resonance will be alleviated since the stator frequency will gradually move away from the resonant range of the CM loop. Therefore, the third-order component $V_{\mathrm{cmi\_3}}$ can be blocked effectively by the CM choke and i_{cm} will reduce consequently. In this case, the control objective should switch from the elimination of $V_{\mathrm{cmi\_3}}$ to the suppression of the PTP magnitude of V_{cmi}. As a result, the PTP value of i_{cm} will be reduced in the high-speed region, which contributes to the reduction of the CM choke size. According to this principle, the V_{cmi} with PTP magnitude suppression in the high-speed region is designed in the cost function as

$$g_{\mathrm{CSI2\_HS}} = \lambda_{V_{\mathrm{cmi}}}\left|V_{\mathrm{cmi}}(k+1)\right|. \tag{27}$$

Finally, the cost function design for the CSI-fed PMSM side is expressed as

$$g_{\mathrm{CSI}} = g_{\mathrm{CSI1}} + g_{\mathrm{CSI2}} \quad g_{\mathrm{CSI2}} = \begin{cases} g_{\mathrm{CSI\_LS}} & \omega_r < \omega_B \\ g_{\mathrm{CSI\_HS}} & \omega_r \geq \omega_B \end{cases} \tag{28}$$

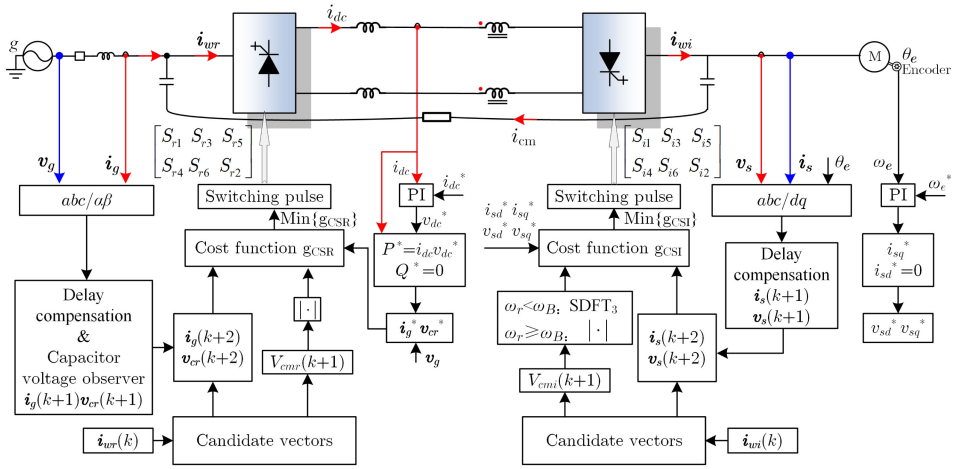

Fig. 5. Proposed FCS-MPC scheme for the CSC-fed PMSM drives with the transformerless operation.

where ω_B is the speed boundary to distinguish whether the motor is running in the low-speed region or the high-speed region.

E. Weighting Factor Recommendation

Both the cost function (17) and (28) have three weighting factors to be tuned. The same tuning procedure can be shared between (17) and (28) due to a similar structure. Therefore, the cost function (17) is used as an example. A lower $\lambda_{V_{cr}}$ cannot damp the filter resonance while the overdamping situation occurs with too larger $\lambda_{V_{cr}}$. Likewise, the increased $\lambda_{V_{\text{cmr}}}$ can maintain a lower PTP magnitude of V_{cmr} but with worse quality of grid current. Therefore, the weighting factor $\lambda_{V_{\text{cr}}}$ and $\lambda_{V_{\text{cmr}}}$ should be tuned according to the tradeoff among grid current reference tracking, filter resonance damping, and V_{cmr} suppression. The tuning process can start from the assumption that the same penalization priority is assigned for different items. With the second-order filtering, the ripple of grid current is much smaller than that of the capacitor voltage. The ripple of the grid current can be roughly estimated as $\Delta V_{cr} T_s / L_r$ by considering the capacitor voltage ripple ΔV_{cr}. Therefore, the square of the ratio of grid current ripple to capacitor voltage ripple can be set as the starting point for $\lambda_{V_{\text{cr}}}$, i.e., ${T_s}^2/{L_r}^2$. Similarly, since the CMV shape is the envelope of capacitor voltage, the tuning of $\lambda_{V_{\text{cmr}}}$ can also start from the same value ${T_s}^2/{L_r}^2$. The performance of each item can be adjusted by further changing the value of weighting factors from the initial point. Finally, the weighting factor λ_{sfr} can be tuned from zero until the desired switching frequency is obtained.

F. Implementation of the Control Scheme

The proposed FCS-MPC scheme for the CSC-fed PMSM drive system is shown in Fig. 5. The PI loop of the CSR side regulates the dc-link current through generating the active power reference, and then the current and capacitor voltage references can be derived. The predictive information of state variables and the value of V_{cmr} can be calculated. Subsequently, the variable $\boldsymbol{i_g}$ and $\boldsymbol{v_{cr}}$ are regulated to track their reference and the PTP magnitude of V_{cmr} value is suppressed via the cost function (17). The full-order observer can estimate $\boldsymbol{v}_{\text{cr}}$ to save hardware costs [29]. For the CSI side, the outer speed loop generates the dq-axis current reference and then the capacitor voltage reference can be calculated. The information of V_{cmi} is predicted by the candidate switching state. The control objective for the CSI side CMV depends on the speed region of the PMSM. When the speed is lower than the defined boundary value ω_B, the CM resonance suppression is prioritized, and thus $V_{\text{cmi\_3}}$ is extracted and then penalized in the cost function. With the increased speed of the PMSM, the CMV control objective switches to the PTP magnitude suppression of V_{cmi}. The regulation of CMV at both CSR and CSI sides provides the freedom to decide which zero vectors should be selected. Thus, the switching state in Table I can be modified in the proposed scheme to further reduce the CMV of the system, i.e., all of the three zero-vectors $\boldsymbol{i_{wr(i)z1}}$, $\boldsymbol{i_{wr(i)z2}}$, and $\boldsymbol{i_{wr(i)z3}}$ can be included in the next interval.

The proposed FCS-MPC scheme takes the advantage of multiobjective optimization for the transformerless CSC-fed drive system. Since both the capacitor voltage of CSR and CSI sides are controlled effectively, the LC/CL filter resonance is mitigated with reduced complexity compared to the existing AD schemes. Moreover, the control scheme concentrates on all CMV generated in the system, while the CM current reduction is the core. Therefore, the size of the CM choke employed in the drive system can be reduced, which saves the cost and improve efficiency.

IV. Simulation Analysis

In order to verify the performance of the proposed FCS-MPC scheme for the transformerless CSC-fed PMSM drives, a simulated system with 1 MVA rated power is realized in the MATLAB/Simulink. The system parameters are shown in Table II. The sampling frequency for the whole system is 12 kHz. Based on the simulated parameters, the weighting factor $\lambda_{V_{\text{cr}}}$ and $\lambda_{V_{\text{cmr}}}$ are tuned from 0.0004 while the adjustment of $\lambda_{V_{\text{ci}}}$ and $\lambda_{V_{\text{cmi}}}$ start from 0.0003. The final weighting factors used in the simulation are $\lambda_{V_{\text{cr}}} = 0.0008$, $\lambda_{V_{\text{cmr}}} = 0.002$, $\lambda_{V_{\text{ci}}} = 0.0015$, and $\lambda_{V_{\text{cmi}}} = 0.001$. The weighting factor λ_{sfr} and λ_{sfi} are tuned to maintain the switching frequency of the CSC are approximately as 1 kHz.

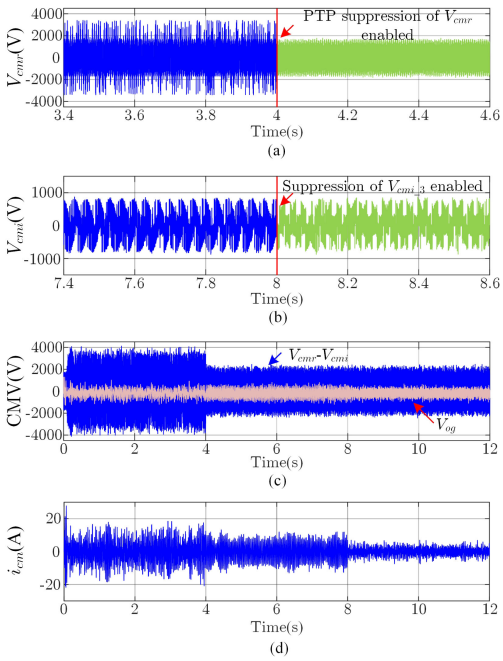

Fig. 6. Simulated performance of the transformerless CSC-fed PMSM system in the low-speed region. From top to bottom: the waveform of V_{cmr} before and after the PTP magnitude suppression, the waveform of V_{cmi} before and after the suppression of $V_{\text{cmi\_3}}$, the CMV waveform of the system with and without the integrated dc-link choke, and the waveform of the CM current.

A. Performance of CM Current in Low-Speed Region

The verification of CM current when PMSM runs in the low-speed region is performed. The rotor speed n_r is kept at 150 r/min and thus the stator frequency is 10 Hz, which implies that V_{cmi} will contain a dominant 30 Hz component and the CM resonance will be amplified at this speed. The load torque is 4000 N · m to simulate the light load and low-speed operation. The arrangement of simulation time is according to the following sequence of events: 1) at the 4 s time instance, the suppression of the PTP magnitude of V_{cmr} is enabled, where the weighting factor $\lambda_{V_{\text{cmr}}}$ changes from 0 to 0.002. Therefore, the effect of the reduced V_{cmr} on the performance of the CM current can be shown; and 2) at the 8 s time instance, the suppression for $V_{\text{cmi\_3}}$ is enabled, where the weighting factor $\lambda_{V_{\text{cmi\_3}}}$ changes from 0 to 0.001. Thus, the reduction of CM current brought by this initiative will be verified.

Fig. 6(a) and (b) shows the waveform of V_{cmr} and V_{cmi}, respectively. As can be seen, the PTP magnitude of V_{cmr} is reduced effectively at the 4 s instance when the penalization item in the cost function is enabled. Consequently, the PTP magnitude of i_{cm} is mitigated, which can be seen in Fig. 6(d). Besides, the suppression of the third-order harmonic $V_{\text{cmi\_3}}$ is realized via the cost function and thus the PTP magnitude of i_{cm} is significantly reduced. To show the effect of the CM choke, the waveform $V_{\text{cmr}} - V_{\text{cmi}}$, which represents the CMV of the system without the CM loop, and V_{og} with the CM loop are compared in Fig. 6(c). It can be seen that the majority of the system CMV is blocked by the CM choke, and thus the voltage stress generated on the motor neutral point is effectively reduced. Since i_{cm} is suppressed by the proposed FCS-MPC scheme, the size of the choke and the CM loop resistance can be eased.

To further verify the improved performance of i_{cm}, Fig. 7 gives the zoom-in view of i_{cm} and the corresponding spectrum using the fast Fourier transform (FFT) analysis. Moreover, the spectrum of the system CMV V_{og} is presented. It can be seen in Fig. 7(a) that without any CMV suppression strategy, the dominant components of i_{cm} are the 30 Hz harmonic and 180 Hz harmonic, which are generated by the $V_{\text{cmi\_3}}$ and $V_{\text{cmr\_3}}$, respectively. The CM current with 180 Hz is blocked because of the relatively large impedance of the CM loop. However, since the resonant frequency of the CM loop is 30 Hz, the CM current at this frequency is amplified. In Fig. 7(b), with the PTP magnitude suppression of V_{cmr}, the low-order harmonics as well as the 180 Hz component of V_{og} are reduced. It can be also found that the magnitude of the 180 Hz component in i_{cm} is approximately reduced by half, and the low-order harmonics are eliminated as well. Furthermore, with the suppression of the third-order harmonic $V_{\text{cmi\_3}}$, the 30 Hz component in V_{og} is reduced significantly. As a result, the CM resonance is attenuated effectively which can be found from the spectrum of i_{cm} in Fig. 7(c). Therefore, with the suppression of the PTP magnitude of V_{cmr} and the third-order harmonic $V_{\text{cmi\_3}}$ concurrently, the magnitude of i_{cm} can be reduced when the motor runs in the low-speed region.

Fig. 8 shows the magnitude of $V_{\text{cmi\_3}}$ and the third-order harmonic of CM current $i_{\text{cm\_3}}$ with and without the suppression of $V_{\text{cmi\_3}}$ when the stator frequency changes from 6 to 20 Hz. First, it can be seen in Fig. 8(a) that the amplitude of $V_{\text{cmi\_3}}$ increases with a higher stator frequency. After the suppression strategy is enabled, the amplitude of $V_{\text{cmi\_3}}$ is significantly reduced, which proves the effectiveness of the proposed FCS-MPC scheme. Moreover, from Fig. 8(b), the most serious CM resonance occurs when the stator frequency is 10 Hz, since the impedance of the CM loop is the smallest (pure resistive). When the frequency increases, the magnitude of $i_{\text{cm\_3}}$ tends to be reduced since the $V_{\text{cmi\_3}}$ is mainly blocked by the CM choke. Therefore, the boundary speed value ω_B can be set as 20 Hz to decide whether the suppression of $V_{\text{cmi\_3}}$ or the PTP magnitude of V_{cmi} should be realized in the cost function at the CSI side.

To further prove that the control objective for the low-speed operation should be the suppression of the $V_{\text{cmi\_3}}$ but not the PTP magnitude of V_{cmi}, Fig. 9 shows the spectrum of i_{cm} and V_{og}, respectively. The spectrum marked in red shows that the suppression of the $V_{\text{cmi\_3}}$ is realized while the spectrum marked in blue means that the suppression objective is the PTP magnitude of V_{cmi}. It can be seen that with the suppression of the $V_{\text{cmi\_3}}$, a better mitigation effect of V_{og} and CM resonance can be achieved when the motor runs in the low-speed region.

B. Performance of CM Current in High-Speed Region

The verification of CM current when PMSM runs at a high-speed is performed. The PMSM runs at 960 r/min speed with 8000 N · m load torque and the stator frequency is 80 Hz. The arrangement of simulation time for the CSR side is the same as the low-speed condition. At the 8 s instance, the CMV

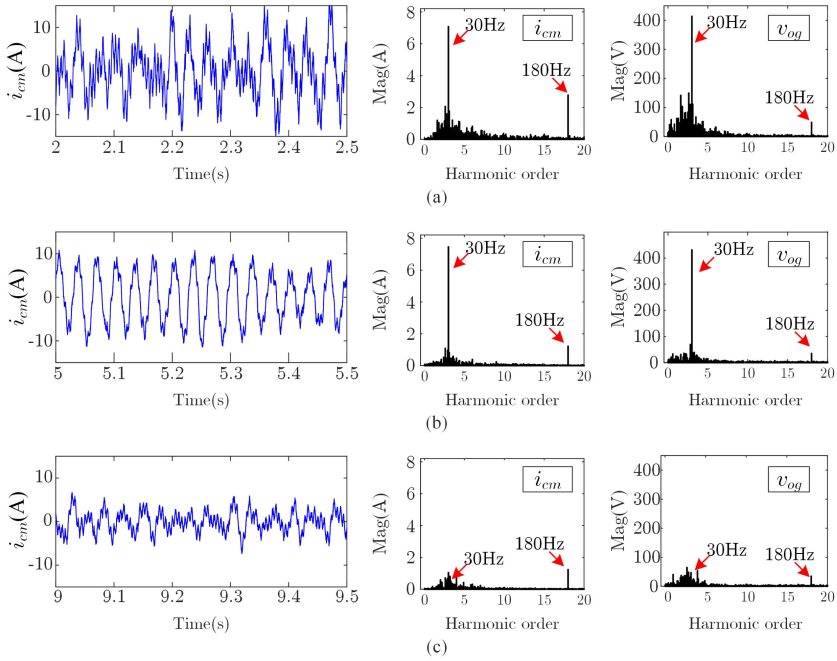

Fig. 7. Waveform of CM current, the corresponding FFT spectrum and FFT spectrum of V_{og} under different CMV scenes. (a) Without suppression of PTP magnitude of V_{cmr} and $V_{\text{cmi\_3}}$. (b) With only the suppression of PTP magnitude of V_{cmr}. (c) With the suppression of PTP magnitude of V_{cmr} and $V_{\text{cmi\_3}}$ simultaneously.

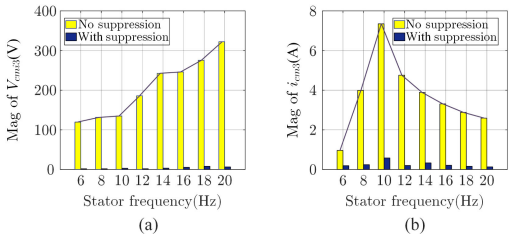

Fig. 8. Comparison of the magnitude of $V_{\text{cmi\_3}}$ and $i_{\text{cm\_3}}$ in the low-speed region with and without the suppression of $V_{\text{cmi\_3}}$.

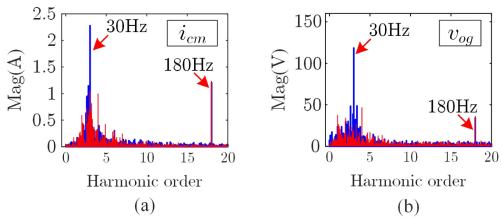

Fig. 9. Spectrum of i_{cm} and V_{og} with the suppression of $V_{\text{cmi\_3}}$ (red) or with the suppression of the PTP magnitude of V_{cmi} (blue) when the stator frequency is 10 Hz.

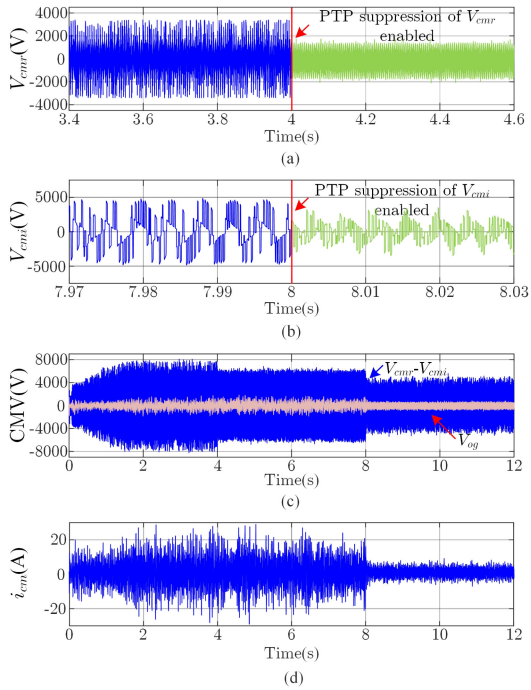

Fig. 10. Simulated performance of the transformerless CSC-fed PMSM system in the high-speed region. From top to bottom: the waveform of V_{cmr} before and after the PTP magnitude suppression, the waveform of V_{cmi} before and after the PTP magnitude suppression, the CMV waveform of the system with and without the integrated dc-link choke, the waveform of the CM current.

penalization item in the cost function of the CSI side is replaced by the suppression of the PTP magnitude of V_{cmi}.

Fig. 10(a) and (b) shows the waveform of V_{cmr} and V_{cmi}, respectively. The PTP magnitude of V_{cmr} and V_{cmi} are reduced, respectively, at the 4 s instance and 8 s instance when the suppression item in the cost function is enabled. With the use of the CM choke, the total CMV of the system V_{og} can be significantly eliminated as seen in Fig. 10(c). Moreover, the magnitude of i_{cm} is reduced accordingly with the reduction of the CMV of both sides, which can be seen in Fig. 10(d).

Fig. 11(a) compares the peak magnitude of V_{cmr}-V_{cmi}, V_{og} and i_{cm} with and without the suppression of the PTP magnitude of CMV at both sides when the stator frequency changes from 30 to 80 Hz. With the suppression of PTP magnitude of V_{cmr} and V_{cmi} enabled, although the CMV V_{cmr}-V_{cmi} without CM choke can be

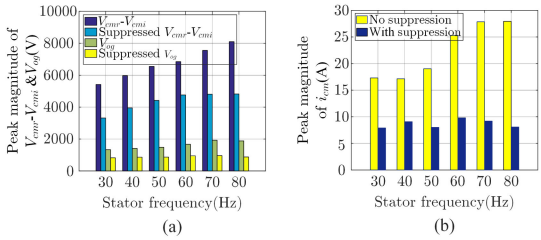

Fig. 11. Comparison of the peak magnitude of V_{cmr}-V_{cmi}, V_{og} and i_{cm} in the high-speed region with and without the suppression of PTP magnitude of CMV at both sides.

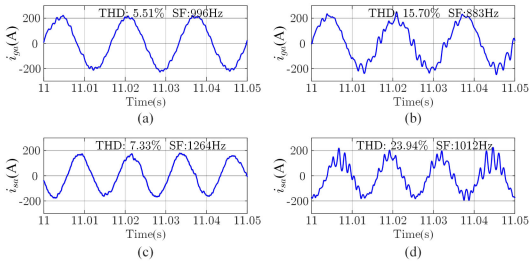

Fig. 12. Comparison of grid and stator current with and without capacitor voltage control for LC/CL resonance suppression. (a) Grid current with capacitor voltage control. (b) Grid current without capacitor voltage control. (c) Stator current with capacitor voltage control. (d) Stator current without capacitor voltage control.

reduced, the voltage stress on the motor is still very high. While with the use of the CM choke and with the effective control strategy for CMV reduction realized, the total voltage stress on the motor can be maintained at a quite low level (almost 10% -15% of V_{cmr} $-V_{\text{cmi}}$). As can be seen in Fig. 11(b), the peak magnitude of i_{cm} can be reduced simultaneously.

To show the effect of LC/CL resonance suppression at both CSR and CSI sides, the waveform of grid current and stator current with and without capacitor voltage feedback control are shown in Fig. 12, respectively. As can be seen, the resonance oscillations are suppressed effectively in the current of both sides, and thus the proposed FCS-MPC scheme can mitigate the LC/CL resonance effectively by regulating the capacitor voltage.

C. Dynamic Performance of CM Current With Speed Change

The proposed FCS-MPC can reduce the CM current effectively for the transformerless operation at steady-state. Two dynamic tests are also performed in Figs. 13 and 14, respectively, which includes the speed change within the low-speed range and the speed changes from the CM resonant region to the high-speed region. As can be seen in Fig. 13, when the stator frequency changes from 10 to 15 Hz, the third-order harmonic component $V_{\text{cmi\_3}}$ is always suppressed and thus the peak value of the CM current is small without large spikes during the dynamic process. In Fig. 14, when the stator frequency further increases to 20 Hz, the magnitude of $V_{\text{cmi\_3}}$ increases a bit since the control objective of the CSI side switches to the PTP magnitude suppression of V_{cmi}. Nevertheless, the peak value of i_{cm} is still maintained at a low level without obvious spikes. Therefore, the proposed

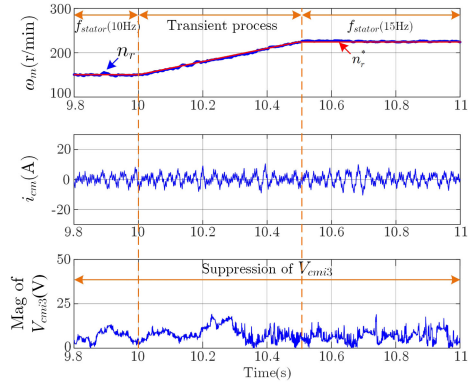

Fig. 13. Dynamic performance of the proposed FCS-MPC when the stator frequency changes from 10 to 15 Hz (the low-speed region).

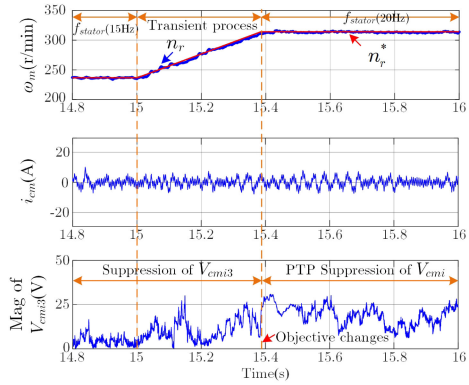

Fig. 14. Dynamic performance of the proposed FCS-MPC when the stator frequency changes from 15 to 20 Hz (The control objective of CSI-side changes from the suppression of $V_{\text{cmi\_3}}$ to the PTP magnitude of V_{cmi}).

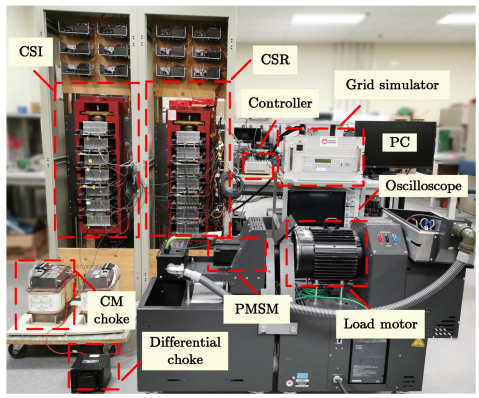

Fig. 15. Experimental setup of the IGCT-based CSC-fed PMSM drive system.

FCS-MPC scheme not only can achieve the desired effect at the steady-state but also maintain a good dynamic performance.

V. Experimental Verification

Fig. 15 shows a scaled IGCT-based hardware prototype for the CSC-fed PMSM drives. The MicroLabBox 1202 controller is employed to verify the proposed FCS-MPC scheme experimentally. The detailed setup parameters are given in Table II. The sampling frequency for the whole system is set as 12 kHz.

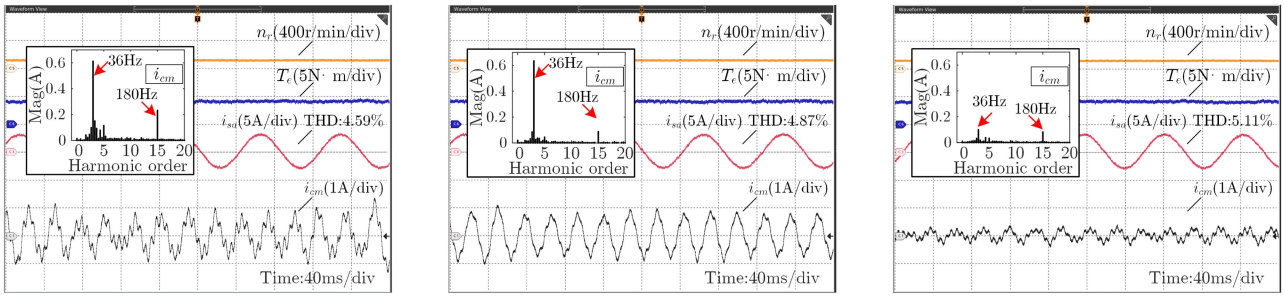

(a) (b) (c)

Fig. 16. Experimental waveform of speed, torque, phase stator current, CM current and the corresponding FFT spectrums of CM current under different CMV scenes. (a) Without suppression of PTP magnitude of V_{cmr} and $V_{\text{cmi\_3}}$. (b) With only the suppression of PTP magnitude of V_{cmr}. (c) With the suppression of PTP magnitude of V_{cmr} and $V_{\text{cmi\_3}}$ simultaneously.

TABLE III
EXPERIMENTAL PARAMETERS OF THE TRANSFORMERLESS DRIVE SYSTEM

	Parameters	Value
CSR	Grid voltage (line-to-line)	90V
	Grid frequency	60Hz
	Line inductance L_r	2.5mH
	Input filter capacitance C_{fr}	160μF
DC link	Differential-mode inductance L_{diff}	40mH
	Common-mode inductance L_{cm}	100mH
	CM resistance R_{cm}	5Ω
	CM resonance frequency f_{cm_res}	32Hz
CSI-PMSM	Output capacitance C_{fi}	120μF
	Rated power of PMSM	1kW
	Rated stator frequency	100Hz
	Stator inductance L_s	3.1mH
	Permanent fluxψ_f	0.15531Wb
	Pole pairsψ_f	5
	Monent of inertia J	0.0012kg·m^2

Based on the experimental parameters, the weighting factor $\lambda_{V_{\text{cr}}}$ and $\lambda_{V_{\text{cmr}}}$ are tuned from 0.0011 while the adjustment of $\lambda_{V_{\text{ci}}}$ and $\lambda_{V_{\text{cmi}}}$ start from 0.0008. The final weighting factors used in the experiment are $\lambda_{V_{\text{cr}}} = 0.001$, $\lambda_{V_{\text{cmr}}} = 0.001$, $\lambda_{V_{\text{ci}}} = 0.0012$, and $\lambda_{V_{\text{cmi}}} = 0.001$.

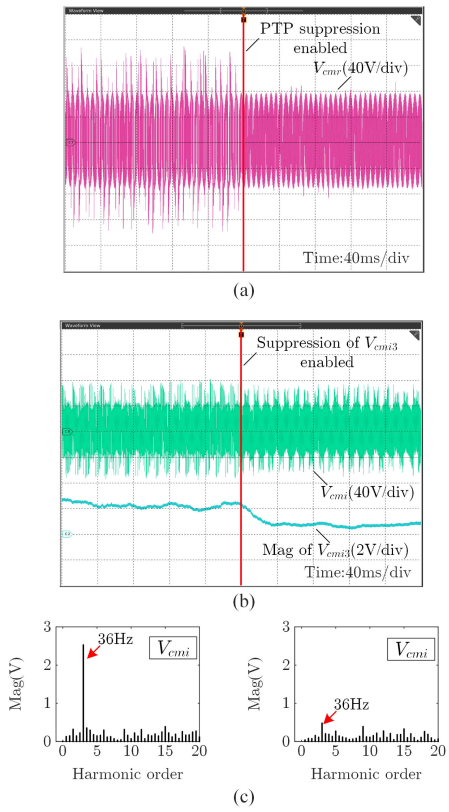

Fig. 17. Experimental CMV of both CSR and CSI before and after suppression strategy in the low-speed region. (a) V_{cmr}. (b) V_{cmi}. (c) The spectrum of V_{cmi}.

A. Experimental Verification in Low-Speed Region

The experimental waveform of speed, torque, phase current, and CM current are shown in Fig. 16 when the PMSM runs with a 12 Hz stator frequency and a 3 N · m load torque. Moreover, the spectrum of the CM current is also presented. It can be seen in Fig. 16(a) that without any CMV suppression strategy, the dominant components of i_{cm} are the 36 Hz harmonic and the 180 Hz harmonic, which are generated by the $V_{\text{cmi\_3}}$ and $V_{\text{cmr\_3}}$, respectively. In Fig. 16(b), It can be also found that the magnitude of the 180 Hz component in i_{cm} is approximately reduced by half with the PTP magnitude suppression of V_{cmr}, and the low-order harmonics are eliminated as well. Furthermore, with the suppression of $V_{\text{cmi\_3}}$, the CM resonance is attenuated effectively, which can be found from the spectrum of i_{cm} in Fig. 16(c). Therefore, when the motor runs in the low-speed region, the CM resonance and the peak of CM current can be reduced effectively by the proposed scheme. Moreover, the total harmonic distortion (THD) of the phase stator current does not change much with the CM current suppression. The stator current performs well without resonance with effective control of the stator voltage.

Fig. 17(a) shows the waveform of V_{cmr}, and the PTP magnitude is reduced after changing the weighting factor $\lambda_{V_{\text{cmr}}}$ from

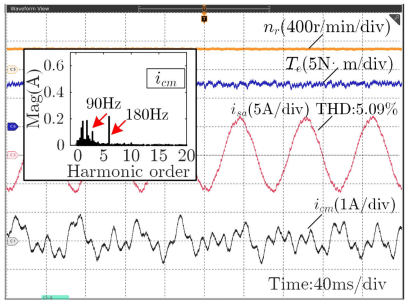

(a)

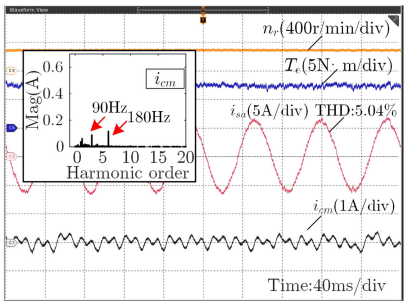

(b)

Fig. 18. Experimental waveform of speed, torque, phase stator current, CM current, and the corresponding FFT spectrums under different CMV scenes with 30 Hz stator frequency. (a) Without suppression of PTP magnitude of V_{cmr} and V_{cmi}. (b) With the suppression of PTP magnitude of V_{cmr} and V_{cmi} simultaneously.

0 to 0.001. The waveform of V_{cmi} and the real-time magnitude of the $V_{\text{cmi\_3}}$ are given in Fig. 17(b). With the weighting factor $\lambda_{V_{\text{cmi\_3}}}$ changed from 0 to 0.0012, the third-order harmonic is reduced, which can also be seen from the spectrum of V_{cmi} in Fig. 17(c).

B. Experimental Verification in High-Speed Region

Fig. 18 shows the experimental waveforms of speed, torque, phase current, and CM current when the PMSM runs at 30 Hz stator frequency and a 6 N · m load torque. First, the spectrum of i_{cm} in Fig. 18(a) is compared with that in Fig. 16(a). This comparison verifies the analysis in Fig. 8(b). It can be seen that the CM resonance has been alleviated with the increased speed, which is the result of the increased loop impedance and the CM choke effectively blocking the third-order component. Therefore, the control objective for the CSI side can switch to the PTP magnitude suppression of V_{cmi}. As can be seen in Fig. 18(b), with the suppression of the PTP magnitude of both V_{cmr} and V_{cmi}, the CM current can be reduced significantly.

Fig. 19 shows the waveform of the grid voltage and the grid current with 1 kHz switching frequency. It can be seen that no LC resonance appears in the current waveform with the capacitor voltage regulation in Fig. 19(a). While in Fig. 19(b), the resonance appears in the grid current without capacitor voltage control. Thus, the proposed cost function can damp the filter resonance effectively.

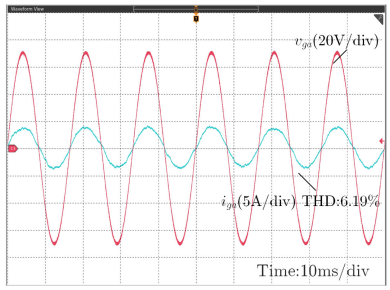

(a)

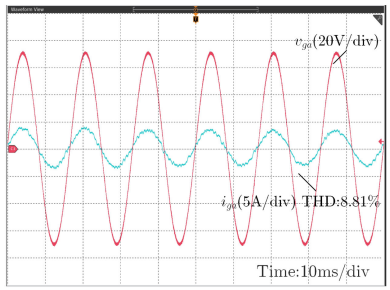

(b)

Fig. 19. Experimental waveform of grid voltage and grid current (a) with capacitor voltage control and (b) without capacitor voltage control.

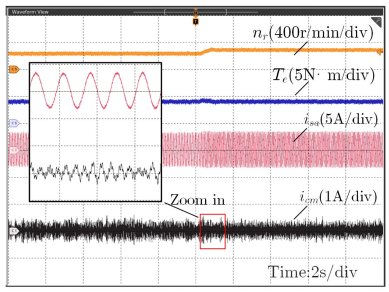

Fig. 20. Dynamic performance of the proposed FCS-MPC when the stator frequency changes from 12 to 15 Hz (the low-speed region).

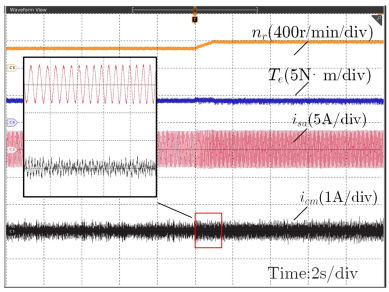

Fig. 21. Dynamic performance of the proposed FCS-MPC when the stator frequency changes from 15 to 20 Hz (the control objective of CSI-side changes from suppression of $V_{\text{cmi\_3}}$ to the PTP magnitude of V_{cmi}).

C. Dynamic Performance Tests of the Proposed Scheme

The experiments for dynamic tests are shown in Figs. 20 and 21, respectively. As can be seen in Fig. 20, with the stator frequency changes from 12 to 15 Hz, the third-order harmonic component is always suppressed and thus the peak value of the

CM current is low without any large spikes during the dynamic process. In Fig. 21, when the stator frequency further increases to 20 Hz, the control objective of the CSI side switches to the PTP magnitude suppression of V_{cmi}, and the peak value of the CM current is still maintained at a low level without obvious spikes.

VI. Conclusion

This article proposes the FCS–MPC scheme applied to the transformerless CSC-fed PMSM drives system. The multiobjective optimization is realized through the designed cost function for both CSR and CSI sides. First, the LC/CL filter resonance is mitigated by directly controlling the capacitor voltage without using the VR-based AD control. Second, the PTP magnitude of the CMV generated from the CSR side is always suppressed. Third, the effect of the CMV generated from the CSI side in different speed ranges is analyzed. In the low-speed range, the control objective suppresses the third-order harmonic of CMV since the CM resonance will be excited. Whereas, in the high-speed range, the CSI side switches to the suppression of the PTP magnitude of CMV. From the simulated results of the 1MVA drive system and the scaled-down experiments, it can be concluded that the proposed MPC with transformerless operation can eliminate the voltage stress on the neutral point of the motor, which is maintained as 10%–15% of the CMV generated by the converter. The CM current is reduced significantly, and thereby the core cross-sectional area, mean length per turn, and total copper loss of the choke can be reduced at least by 60%, 37%, 22.25%, respectively, if a toroid core is adopted. Besides, the LC/CL resonance can be mitigated effectively for both CSR and CSI sides, respectively, with enhanced system stability. The proposed FCS-MPC can be applied to motor drives where the background shares similar problems, i.e., the CMV reduction and CM resonance suppression.

References

[1] B. Wu, *High-Power Converters and Ac Drives*, Hoboken, NJ, USA: Wiley, 2017.

[2] H. Abu-Rub, S. Bayhan, S. Moinoddin, M. Malinowski, and J. Guzinski, "Medium-voltage drives: Challenges and existing technology," *IEEE Power Electron. Mag*., vol. 3, no. 2, pp. 29–41, Jun. 2016.

[3] H. Abu-Rub, J. Holtz, J. Rodriguez, and G. Baoming, "Medium-voltage multilevel converters-state of the art, challenges, and requirements in industrial applications," *IEEE Trans. Ind. Electron.*, vol. 57, no. 8, pp. 2581–2596, Aug. 2010.

[4] B. Wu, J. Pontt, J. Rodriguez, S. Bernet, and S. Kouro, "Current-source converter and cycloconverter topologies for industrial medium-voltage drives," *IEEE Trans. Ind. Electron*., vol. 55, no. 7, pp. 2786–2797, Jul. 2008.

[5] M. Malinowski and S. Bernet, "A simple voltage sensorless active damping scheme for three-phase PWM converters with an LCL filter," *IEEE Trans. Ind. Electron*., vol. 55, no. 4, pp. 1876–1880, Apr. 2008.

[6] J. Dannehl, M. Liserre, and F. W. Fuchs, "Filter-based active damping of voltage source converters with LCL filter," *IEEE Trans. Ind. Electron*., vol. 58, no. 8, pp. 3623–3633, Aug. 2011.

[7] J. He and Y. W. Li, "Generalized closed-loop control schemes with embedded virtual impedances for voltage source converters with LC or LCL filters," *IEEE Trans. Power Electron*., vol. 27, no. 4, pp. 1850–1861, Apr. 2012.

[8] Z. Bai, H. Ma, D. Xu, B. Wu, Y. Fang, and Y. Yao, "Resonance damping and harmonic suppression for grid-connected current-source converter," *IEEE Trans. Ind. Electron*., vol. 61, no. 7, pp. 3146–3154, Jul. 2014.

[9] Y. W. Li, "Control and resonance damping of voltage-source and current-source converters with LC filters," *IEEE Trans. Ind. Electron*., vol. 56, no. 5, pp. 1511–1521, May 2009.

[10] H. Lee, S. Jung, and S. Sul, "A current controller design for current source inverter-fed ac machine drive system," *IEEE Trans. Power Electron*., vol. 28, no. 3, pp. 1366–1381, Mar. 2013.

[11] J. C. Wiseman and Bin Wu, "Active damping control of a high-power PWM current-source rectifier for line-current THD reduction," *IEEE Trans. Ind. Electron*., vol. 52, no. 3, pp. 758–764, Jun. 2005.

[12] Z. Wang, B. Wu, D. Xu, and N. R. Zargari, "Hybrid PWM for high-power current-source-inverter-fed drives with low switching frequency," *IEEE Trans. Power Electron*., vol. 26, no. 6, pp. 1754–1764, Jun. 2011.

[13] G. Jaroslaw, H. Abu-Rub, and P. Strankowski, "*Variable Speed Ac Drives With Inverter Output Filters*," Hoboken, NJ, USA: John Wiley and Sons, 2015.

[14] F. DeWinter, N. Zargari, S. Rizzo, and Yuan Xiao, "Medium voltage drives: Are isolation transformers required?" in *Rec. Conf. Papers Ind. Appl. Soc., 49th Annu. Conf. Petroleum Chem. Ind. Tech. Conf.*, 2002, pp. 191–196.

[15] A. M. Hava and E. Ün, "A high-performance PWM algorithm for common-mode voltage reduction in three-phase voltage source inverters," *IEEE Trans. Power Electron*., vol. 26, no. 7, pp. 1998–2008, Jul. 2011.

[16] Hee-Jung Kim, Hyeoun-Dong Lee, and Seung-Ki Sul, "A new PWM strategy for common-mode voltage reduction in neutral-point-clamped inverter-fed ac motor drives," *IEEE Trans. Ind. Appl*., vol. 37, no. 6, pp. 1840–1845, Nov./Dec. 2001.

[17] M. J. Duràn, J. Prieto, F. Barrero, J. A. Riveros, and H. Guzman, "Space-vector PWM with reduced common-mode voltage for five-phase induction motor drives," *IEEE Trans. Ind. Electron*., vol. 60, no. 10, pp. 4159–4168, Aug. 2013.

[18] N. Zhu, D. Xu, B. Wu, N. R. Zargari, M. Kazerani, and F. Liu, "Common-mode voltage reduction methods for current-source converters in medium-voltage drives," *IEEE Trans. Power Electron*., vol. 28, no. 2, pp. 995–1006, Feb. 2013.

[19] J. Shang, Y. W. Li, N. R. Zargari, and Z. Cheng, "PWM strategies for common-mode voltage reduction in current source drives," *IEEE Trans. Power Electron*., vol. 29, no. 10, pp. 5431–5445, Oct. 2014.

[20] Bin Wu, S. Rizzo, N. Zargari, and Y. Xiao, "An integrated dc link choke for elimination of motor common-mode voltage in medium voltage drives," in *Conf. Record IEEE Ind. Appl. Conf. 36th IAS Annu. Meeting (Cat. No.01CH37248)*, vol. 3, 2001, pp. 2022–2027.

[21] Y. Lian, Y. Zhang, Y. Wei Li, N. R. Zargari, and Z. Cheng, "Common-mode resonance suppression in transformerless PWM current-source drive," *IEEE Trans. Power Electron*., vol. 31, no. 8, pp. 5721–5731, 2016.

[22] L. Ding, Z. Quan, and Y. W. Li, "Common-mode voltage reduction for parallel CSC-fed motor drives with multilevel modulation," *IEEE Trans. Power Electron*., vol. 33, no. 8, pp. 6555–6566, Aug. 2018.

[23] L. Ding and Y. W. Li, "Simultaneous dc current balance and common-mode voltage control with multilevel current source inverters," *IEEE Trans. Power Electron*., vol. 33, no. 11, pp. 9188–9197, Nov. 2018.

[24] S. Vazquez, J. Rodriguez, M. Rivera, L. G. Franquelo, and M. Norambuena, "Model predictive control for power converters and drives: Advances and trends," *IEEE Trans. Ind. Electron*., vol. 64, no. 2, pp. 935–947, Feb. 2017.

[25] S. Kouro, P. Cortes, R. Vargas, U. Ammann, and J. Rodriguez, "Model predictive control-a simple and powerful method to control power converters," *IEEE Trans. Ind. Electron*., vol. 56, no. 6, pp. 1826–1838, Jun. 2009.

[26] H. Gao, B. Wu, D. Xu, M. Pande, and R. P. Aguilera, "Common-mode-voltage-reduced model-predictive control scheme for current-source-converter-fed induction motor drives," *IEEE Trans. Power Electron*., vol. 32, no. 6, pp. 4891–4904, Jun. 2017.

[27] Y. Lian, Y. W. Li, Z. Quan, N. R. Zargari, and Z. Cheng, "SVM strategies for common-mode current reduction in transformerless current-source drives at low modulation index," *IEEE Trans. Power Electron*., vol. 32, no. 2, pp. 1312–1323, Feb. 2017.

[28] P. Cortes, J. Rodriguez, C. Silva, and A. Flores, "Delay compensation in model predictive current control of a three-phase inverter," *IEEE Trans. Ind. Electron*., vol. 59, no. 2, pp. 1323–1325, Feb. 2012.

[29] C. Xue, L. Ding, Y. Li, and N. R. Zargari, "Improved model predictive control for high-power current-source rectifiers under normal and distorted grid conditions," *IEEE Trans. Power Electron.*, vol. 35, no. 5, pp. 4588–4601, May 2020.

[30] E. Jacobsen and R. Lyons, "The sliding DFT," *IEEE Signal Process. Mag*., vol. 20, no. 2, pp. 74–80, Mar. 2003.

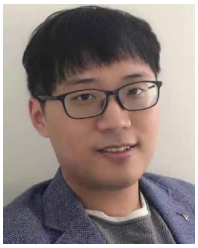

Cheng Xue (Student Member, IEEE) received the B.Eng. (Yisheng Mao hons.) and M.Sc. degrees in electrical engineering from Southwest Jiaotong University, Chengdu, China, in 2015 and 2018, respectively. He is currently working toward the Ph.D. degree with the Department of Electrical and Computer Engineering, University of Alberta, Edmonton, AB, Canada.

His research interests include electrical machine drives and advanced control of power electronic converters.

Li Ding (Member, IEEE) received the B.Eng. degree from Shanghai University, Shanghai, China, in 2013, the M.Sc. degree from the Harbin Institute of Technology, Harbin, China, in 2015, and the Ph.D. degree from the University of Alberta, Edmonton, AB, Canada, in 2020, all in electrical engineering.

He is currently a Postdoctoral Research Fellow with the Department of Electrical and Computer Engineering, University of Alberta. His research interests include current-source converters, sensorless motor drives, wide band-gap devices, and parameter identification.

Yunwei (Ryan) Li (Fellow, IEEE) received the B.Sc. Eng. degree in electrical engineering from Tianjin University, Tianjin, China, in 2002, and the Ph.D. degree from Nanyang Technological University, Singapore, in 2006.

In 2005, he was a Visiting Scholar with Aalborg University, Aalborg, Denmark. From 2006 to 2007, he was a Post Doctoral Research Fellow with Ryerson University, Toronto, ON, Canada. In 2007, he was with Rockwell Automation, Cambridge, ON, Canada, and the University of Alberta, Edmonton, AB, Canada, where he is currently a Professor. His research interests include distributed generation, microgrid, renewable energy, high-power converters, and electric motor drives.

Dr. Li serves as an Editor-in-Chief for the IEEE TRANSACTIONS ON POWER ELECTRONICS LETTERS. Prior to that, he was an Associate Editor for the IEEE TRANSACTIONS ON POWER ELECTRONICS, IEEE TRANSACTIONS ON INDUSTRIAL ELECTRONICS, IEEE TRANSACTIONS ON SMART GRID, and IEEE JOURNAL OF EMERGING AND SELECTED TOPICS IN POWER ELECTRONICS. He was the recipient of the Richard M. Bass Outstanding Young Power Electronics Engineer Award from the IEEE Power Electronics Society in 2013 and the Second Prize Paper Award for the IEEE TRANSACTIONS ON POWER ELECTRONICS in 2014. He is listed as a Highly Cited Researcher by the Web of Science Group.